Wideband microwave measurements of the extinction cross section---Experimental techniques

Larsson, Christer; Gustafsson, Mats; Kristensson, Gerhard

2009

CODEN:LUTEDX/(TEAT-7182)/1-22/(2009)

Wideband microwave measurements of the extinction cross section—Experimental techniques

Christer Larsson, Mats Gustafsson, and Gerhard Kristensson

Electromagnetic Theory
Department of Electrical and Information Technology
Lund University
Sweden

Mats Gustafsson, and Gerhard Kristensson
{Mats.Gustafsson,Gerhard.Kristensson}@eit.lth.se

Department of Electrical and Information Technology
Electromagnetic Theory
Lund University
P.O. Box 118
SE-221 00 Lund
Sweden

Christer Larsson
Christer.Larsson@saabgroup.com
Christer.Larsson@eit.lth.se

Saab Bofors Dynamics AB
SE-581 88 Linköping
Sweden

Department of Electrical and Information Technology
Electromagnetic Theory
Lund University
P.O. Box 118
SE-221 00 Lund
Sweden

Editor: Gerhard Kristensson

Abstract

This paper describes the development of a method to determine the extinction cross section for a very large bandwidth in the microwave region. The method is based on measurements of the radar cross section in the forward direction to calculate the extinction cross section for the frequency range [2.5, 38] GHz. The method is applicable to samples of arbitrary shape and composition and can also be used for polarimetric measurements. Coherent background subtraction is used to remove the contribution from antenna to antenna coupling. Time domain gating is employed to increase the sensitivity. Different calibration methods are discussed. The efficiency of the background subtraction and the accuracy of the measurements are estimated.

1 Introduction

The motivation for this study is to develop an experimental method that can be used to verify recent theoretical work, which shows that the extinction cross section integrated over all frequencies is related to the static properties of the scatterer, see Refs. 8, 20, 21. A method based on polarimetric measurements of the radar cross section (RCS) in the forward direction is therefore developed in order to verify the theoretical work. The optical theorem is used to calculate the extinction cross section from the measured forward RCS for arbitrary polarization of the incident radiation. The method described in this paper can be applied to samples of arbitrary shape and composition. This can be compared to the previously reported method based on monostatic RCS measurements which was restricted to thin planar surfaces at normal incidence, see Refs 14, 21.

Forward RCS measurement ranges and measurements are less common than monostatic RCS ranges and measurements. There are several probable reasons for this. One reason is that most radar applications are monostatic. An important advantage of forward scattering and other bistatic radar systems is that they can be used to detect objects which have a low monostatic radar signature, see Ref. 23. In fact, shaping, which is a common method to reduce the monostatic RCS, is not an efficient method to reduce the forward RCS. The forward RCS is mainly a function of geometric cross section area regardless of shape, when the target is large compared to the wavelength, see Ref. 12. The forward RCS cannot be reduced significantly by radar absorbing materials either, see Ref. 18. The disadvantage of forward scattering and other bistatic radar systems is that they are in general more complicated than monostatic systems, *e.g.*, instead of one location for the monostatic system a bistatic system requires two locations and time synchronization between the locations. Some applications that use scattering in the forward direction are systems for ground target identification, see Ref. 3, and radar fences, see Ref. 23. The relative lack of applications where forward scattering is used means that most RCS measurement ranges are set up for monostatic measurements.

Another reason for the relative scarcity of forward RCS ranges and measurements is that forward RCS measurements in the laboratory are technically complicated due to the large direct contribution from the transmitting antenna to the received

signal. The direct contribution to the signal has to be removed using coherent subtraction. This puts considerable demands on the dynamic range and the stability of the system.

There are only a few measurement ranges designed for forward RCS measurements described in the open literature. A system where the RCS in the forward direction can be measured is described in Ref. 4. That system operates in the [2, 12.4] GHz range with a measurement accuracy of 1 dB at a level of –18 dBsm for the forward RCS.

An anechoic chamber, originally designed for monostatic RCS measurements, is rearranged for polarimetric forward RCS measurements in the work described in the present paper. The measurement setup is described and two different calibration methods that can be used for the forward scattering measurements are evaluated. The efficiency of the data processing methods that are used, coherent background subtraction and time domain gating, are determined and discussed. The accuracy of the measured forward RCS and the extinction cross section is estimated by comparing with calculations.

2 Theory

Consider the direct scattering problem of a time harmonic plane electromagnetic wave impinging in the $\hat{\boldsymbol{k}}$-direction on a bounded scatterer. The bistatic RCS, $\sigma(f, \hat{\boldsymbol{r}})$, in the $\hat{\boldsymbol{r}}$ direction at the frequency f is then defined as, see Ref. 11,

$$\sigma(f, \hat{\boldsymbol{r}}) = \lim_{r \to \infty} 4\pi r^2 \frac{|\boldsymbol{E}_{\mathrm{s}}(\boldsymbol{r})|^2}{|\boldsymbol{E}_{\mathrm{i}}|^2}, \tag{2.1}$$

where $\boldsymbol{E}_{\mathrm{i}}$ denotes the incident electric field, $\boldsymbol{E}_{\mathrm{s}}$ denotes the scattered electric field and $r = |\boldsymbol{r}|$ denotes the magnitude of the position vector $\boldsymbol{r} = r\hat{\boldsymbol{r}}$. Introduce the complex-valued bistatic RCS amplitude, $\boldsymbol{A}(f, \hat{\boldsymbol{r}})$, in the $\hat{\boldsymbol{r}}$ direction. $\boldsymbol{A}(f, \hat{\boldsymbol{r}})$ preserves the phase information in the measurement and it is defined as,

$$\boldsymbol{A}(f, \hat{\boldsymbol{r}}) = \lim_{r \to \infty} 2\sqrt{\pi} r \frac{\boldsymbol{E}_{\mathrm{s}}^*(\boldsymbol{r})}{|\boldsymbol{E}_{\mathrm{i}}|} \mathrm{e}^{-\mathrm{i}kr}, \tag{2.2}$$

where it is assumed that the time convention is $\mathrm{e}^{-\mathrm{i}\omega t}$ for the time harmonic wave and $k = 2\pi f/\mathrm{c}_0$. c_0 is the phase velocity of light in free space.

$\sigma(f, \hat{\boldsymbol{r}})$ and $\boldsymbol{A}(f, \hat{\boldsymbol{r}})$ are then related by,

$$\sigma(f, \hat{\boldsymbol{r}}) = |\boldsymbol{A}(f, \hat{\boldsymbol{r}})|^2. \tag{2.3}$$

In practice, the two polarization components of $\boldsymbol{A}(f, \hat{\boldsymbol{r}})$ are measured separately for an incident wave that is transmitted with a defined polarization in most RCS measurements. This means that measured RCS data usually is presented as a function of the transmitted and received polarizations used in the measurement, see Ref. 10. As an example, σ_{VH} and A_{VH} would be the notations for the recorded RCS and RCS amplitude component, respectively, for vertical transmitting and horizontal receiving linear polarizations.

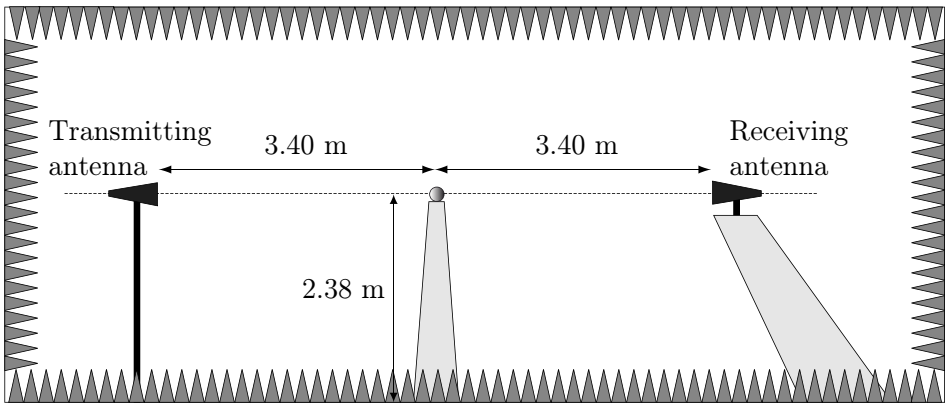

Figure 1: The figure shows the experimental setup in the anechoic chamber.

The scattering cross section, $\sigma_{\mathrm{s}}(f)$, is the average of the bistatic RCS over all angles, *i.e.*, integration over the unit sphere Ω, namely,

$$\sigma_{\mathrm{s}}(f) = \frac{1}{4\pi} \int_{\Omega} \sigma(f, \hat{\boldsymbol{r}}) \, \mathrm{d}\Omega, \tag{2.4}$$

where $\mathrm{d}\Omega$ denotes the surface element of the unit sphere. The extinction cross section, $\sigma_{\mathrm{ext}}(f)$, sometimes also designated the total cross section, see Ref. 17, is defined as

$$\sigma_{\mathrm{ext}}(f) = \sigma_{\mathrm{s}}(f) + \sigma_{\mathrm{a}}(f), \tag{2.5}$$

where $\sigma_{\mathrm{a}}(f)$ is the absorption cross section, which is a measure of the power absorbed by the scatterer, see Ref. 2. The extinction cross section can be determined using (2.5) by measuring the bistatic RCS at all angles and the absorption cross section. However, a more straightforward method is to measure the RCS amplitude in the forward direction, $\boldsymbol{A}(f, \hat{\boldsymbol{k}})$, and use the optical theorem to determine $\sigma_{\mathrm{ext}}(f)$, see Ref. 16,

$$\sigma_{\mathrm{ext}}(f) = \frac{\mathrm{c}_0}{\sqrt{\pi} f} \operatorname{Im} A_{\mathrm{ii}}(f, \hat{\boldsymbol{k}}), \tag{2.6}$$

where $A_{\mathrm{ii}}(f, \hat{\boldsymbol{k}})$ is the component of $\boldsymbol{A}(f, \hat{\boldsymbol{k}})$ that is co-polarized with the incident electric field, $\boldsymbol{E}_{\mathrm{i}}$, *i.e.*,

$$A_{\mathrm{ii}}(f, \hat{\boldsymbol{k}}) = \boldsymbol{A}(f, \hat{\boldsymbol{k}}) \cdot \frac{\boldsymbol{E}_{\mathrm{i}}}{|\boldsymbol{E}_{\mathrm{i}}|} \tag{2.7}$$

The optical theorem thus makes it possible to determine the extinction cross section by a measurement of the RCS amplitude in the forward direction.

3 Measurements

3.1 Near and farfield measurements

In an ideal RCS measurement a plane wave impinges on the target. However, this is not the case in a practical measurement where a finite distance between antenna and

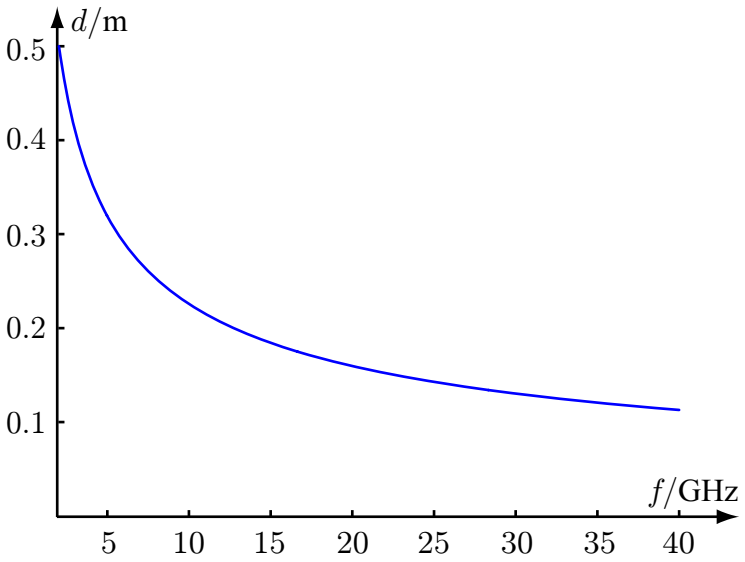

Figure 2: The largest transverse size of the object in order to fulfill the criterion in (3.1).

target has to be used. With increasing distance the spherical wave becomes more and more like a plane wave over the target. On the other hand, as the distance increases so do practical problems and cost. The question then becomes: How large distance is needed for the RCS measurement of a certain target and how much will the chosen distance contribute to measurement error? This problem does not have a general solution valid for all targets. Different analyses show, see Refs. 11, 13, 17, that if the phase difference over the target is less than $\pi/8$, then the error in the RCS-measurement due to the spherical wavefront is less than 1 dB for most targets. This requirement on the phase deviation over a target of size d gives the relation,

$$r > \frac{2d^2}{\lambda}, \tag{3.1}$$

where λ is the wavelength of the incident radiation and r is the distance between antenna and target. (3.1) is commonly referred to as the Far-field criterion, see Ref. 11. It is commonly used to determine the necessary antenna to target distance for an RCS-measurement.

Rewriting (3.1) gives a restriction for the maximum size of the measured objects that can be used in a measurement setup with a fixed distance between antenna and target.

$$d < \sqrt{\frac{r\mathrm{c}_0}{2f}}, \tag{3.2}$$

where f is the frequency and c_0 is the speed of light. The measurement system geometry is shown in Figure 1. Using this measurement distance, r=3.40 m, and frequency range of interest for this work, Figure 2 is obtained. Figure 2 shows that measurements that are within the limits given by the far field criterion can be

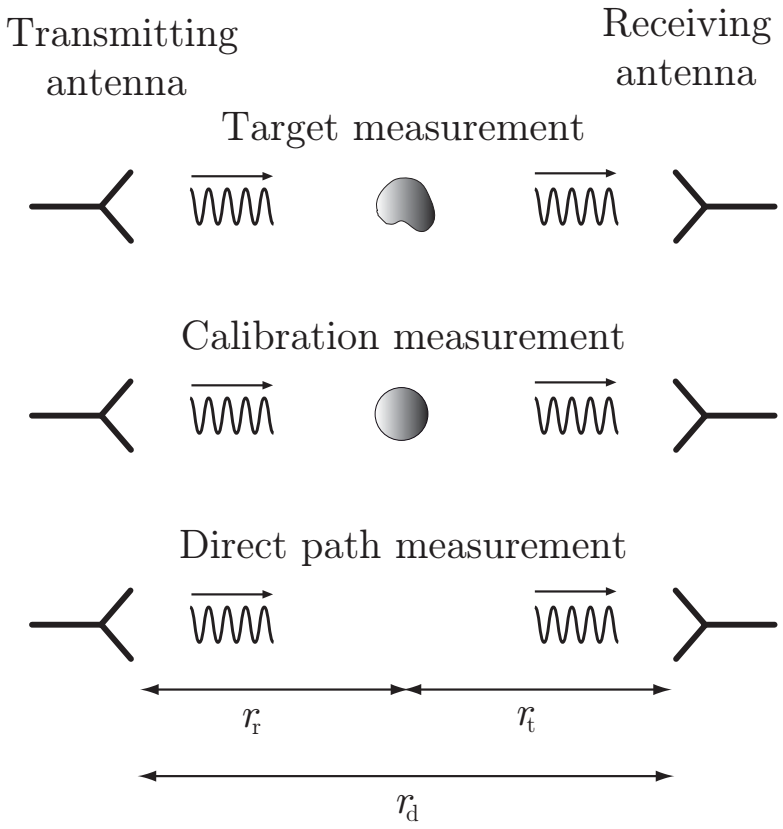

Figure 3: The three different measurement setups that are considered.

performed on samples that are smaller than 0.16 m and 0.11 m for measurements up to 18 and 38 GHz, respectively.

3.2 Calibration

Calibration is a crucial component in all RCS measurements. The quality of the calibration and the accuracy inherent in the calibration procedure have large impact on the quality of the calibrated data acquired from the measurement. It is therefore useful to analyze the different methods that can be used in some detail.

Two calibration methods are considered in this section using different combinations of the measurement setups shown in Figure 3. The first method is the traditional calibration method used in most RCS measurements. It uses a target with known RCS as a calibration target to calibrate the target measurement. The second method that is described here does not require a calibration target. It uses a direct path measurement of the signal to calibrate the target measurement. This is a feature which can be useful for many setups. To the best of our knowledge, the latter method is not in frequent use in the RCS community. The following discussion on calibration is restricted to forward scattering, *i.e.*, $\hat{\boldsymbol{r}} = \hat{\boldsymbol{k}}$, but can be generalized to other directions as well.

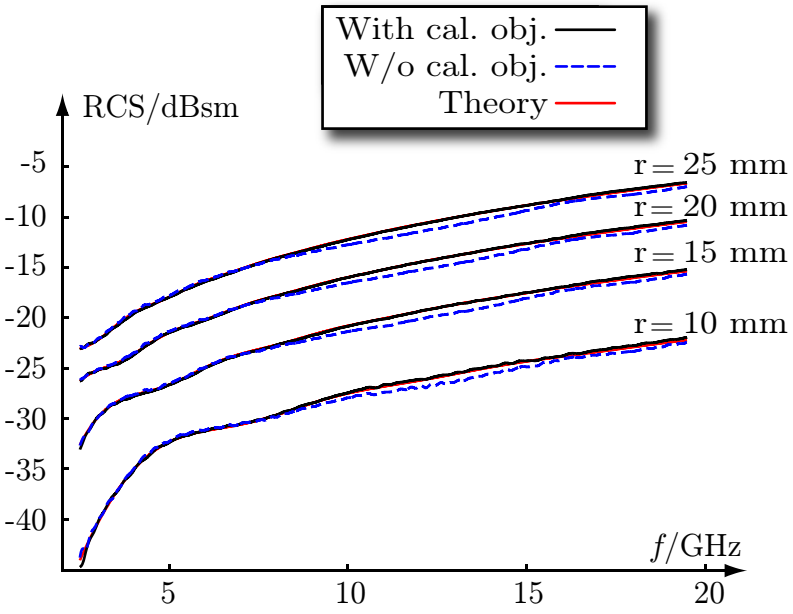

Figure 4: Comparison between results from forward RCS measurements on metal spheres using the two calibration methods described here. The RCS obtained from Mie series calculation is shown as a reference.

3.2.1 Calibration using a calibration target

The first calibration method that is described here, calibration using a calibration target, is the standard method for RCS calibration. It is described in detail in a number of sources, see *e.g.*, Refs. 5, 11. The main features of this method are outlined in this section.

Starting with one of many formulations of the radar equation, see Ref. 19, an RCS measurement can be described by,

$$P_{\mathrm{r}}(f) = \frac{P_{\mathrm{t}}(f)G_{\mathrm{t}}(f)}{4\pi r_{\mathrm{t}}^2}\frac{\sigma(f)}{4\pi r_{\mathrm{r}}^2}\frac{G_{\mathrm{r}}(f)\lambda^2}{4\pi}\frac{1}{L(f)}, \tag{3.3}$$

where $P_{\mathrm{r}}(f)$ is the power received at the receiving antenna, $P_{\mathrm{t}}(f)$ is the power transmitted, $G_{\mathrm{t}}(f)$ is the gain of the transmitting antenna, $\sigma(f)$ is the RCS for the target, $G_{\mathrm{r}}(f)$ is the gain of the receiving antenna, r_{t} is the distance between the transmitting antenna and the target to be measured, r_{r} is the distance between the target to be measured and the receiving antenna, λ is the wavelength of the radiation and $L(f)$ is the system losses in cables etc. The power measures, the gains and the loss are not normalized in this stage of the measurement.

If the system is kept constant without change of geometry and hardware setup, only allowing the change between different targets, then all parameters in (3.3) except $\sigma(f)$ can be replaced by a parameter that only depends on f, $K(f)$,

$$P_{\mathrm{r}}(f) = K(f)\sigma(f). \tag{3.4}$$

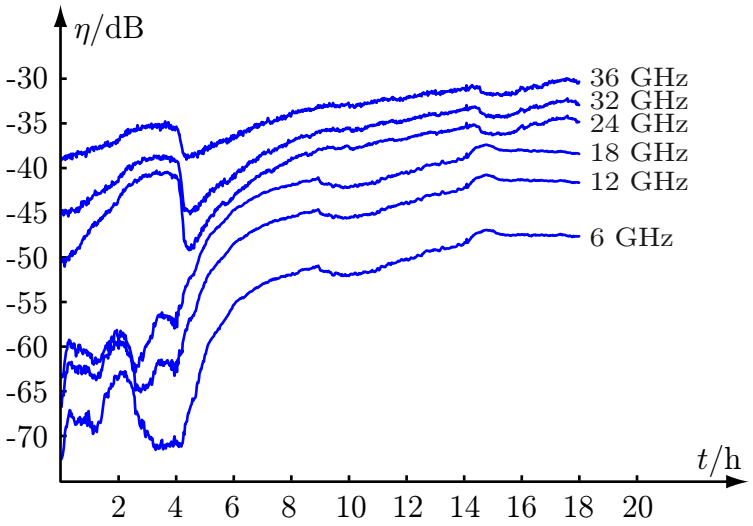

Figure 5: The figure shows the subtraction efficiency as a function of time, in hours, for $2\Delta f = 2\,\mathrm{GHz}$ wide frequency bands. The curves are labeled with the center frequencies of the frequency bands.

This leads to

$$\sigma(f) = \frac{P_{\mathrm{r}}(f)}{K(f)}. \tag{3.5}$$

In practice, coherent radar measurements are performed to determine the separate polarization components of the RCS amplitude, A_{ij},

$$A_{\mathrm{ij}}(f) = v_{\mathrm{cal}}(f) V_{\mathrm{ij,r}}(f), \tag{3.6}$$

where $v_{\mathrm{cal}}(f)$ is a complex-valued quantity that is sometimes referred to as a calibration vector, and $V_{\mathrm{ij,r}}(f)$ is the complex-valued amplitude as measured at the receiver. $v_{\mathrm{cal}}(f)$ has to be determined in a calibration measurement using a target with known RCS amplitude, $A_{\mathrm{ij,cal}}(f)$.

$$v_{\mathrm{cal}}(f) = \frac{A_{\mathrm{ij,cal}}(f)}{V_{\mathrm{ij,r,cal}}(f)}, \tag{3.7}$$

where $V_{\mathrm{ij,r,cal}}(f)$ is the amplitude at the receiver of the calibration target.

Metallic spheres are used as calibration objects for all the measurements that are presented in this paper. Spheres are ideal calibration objects for several reasons, as pointed out in Ref. 4. The RCS in the forward direction is easy to calculate to very good accuracy using the Mie series, see Ref. 17. The symmetry of a sphere means that it is straightforward to align it. A sphere has also a much larger forward RCS than its monostatic RCS. In fact, a sphere's forward RCS is similar to the forward RCS of a flat plate with the same cross section area.

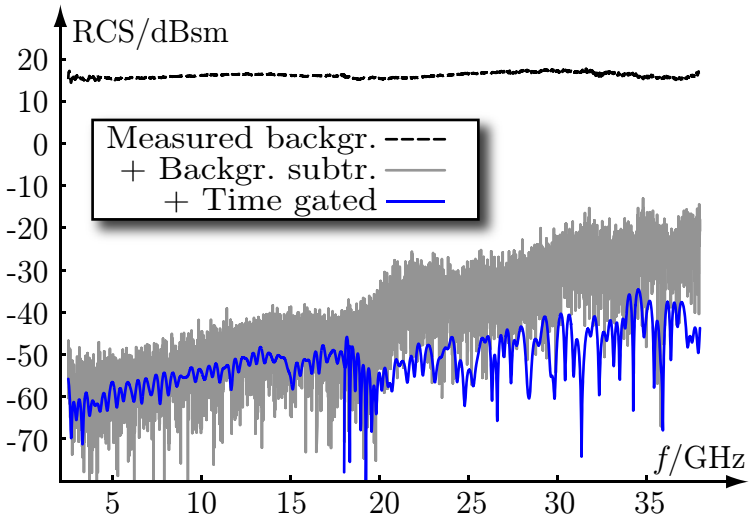

Figure 6: Measurement of the background. The figure shows calibrated raw data from a background measurement, data after subtracting another background measurement, and after additional time gating.

3.2.2 Calibration without calibration target

In some cases, finding and utilizing an accurate calibration target is complicated. Especially for bistatic geometries this can be a problem. It is therefore of interest to find a method that does not require a calibration target. Only a few descriptions of a method that does not use a calibration target are found in the literature, which indicates that it is not very common and certainly much less frequently used than the calibration using a calibration target.

This alternative method is based on measuring the direct signal from transmitting to receiving antenna. In Ref. 1 this procedure is used to calibrate forward scattering measurements from different terrain types. The basic details are outlined in Ref. 6 where the method is used to calibrate the measurements in an outdoors bistatic RCS range. The method is also described and discussed in great detail in Ref. 24 and test measurements on simple targets are performed in Ref. 25.

The transmitting and receiving antennas are positioned facing each other so that the direct path signal can be measured. The radar equation then becomes

$$P_{\mathrm{d}}(f) = \frac{P_{\mathrm{t}}(f)G_{\mathrm{t}}(f)}{4\pi r_{\mathrm{d}}^2}\frac{G_{\mathrm{r}}(f)\lambda^2}{4\pi}\frac{1}{L(f)}, \tag{3.8}$$

where $P_{\mathrm{d}}(f)$ is the measured direct path power and r_{d} is the distance between the transmitting and receiving antennas. (3.8) can be rewritten in the following form

$$P_{\mathrm{d}}(f)4\pi r_{\mathrm{d}}^2 = P_{\mathrm{t}}(f)G_{\mathrm{t}}(f)\frac{G_{\mathrm{r}}(f)\lambda^2}{4\pi}\frac{1}{L(f)}, \tag{3.9}$$

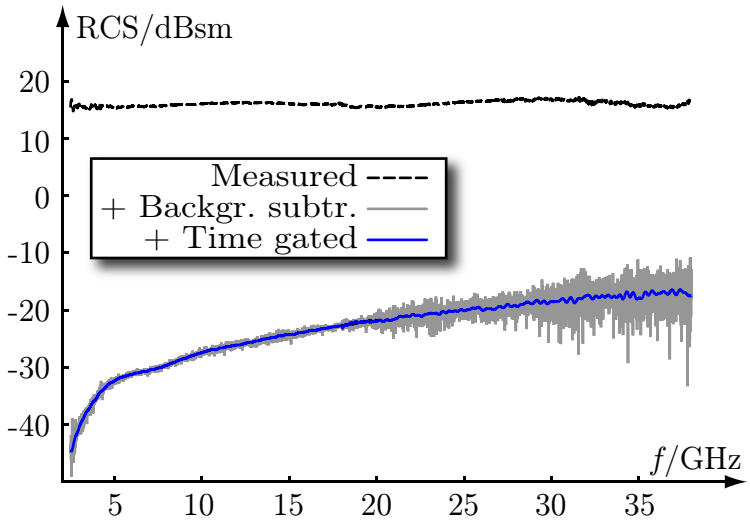

Figure 7: Measurement of the forward RCS of a metal sphere with 10 mm radius. The figure shows calibrated raw data, data after background subtraction and the data after time domain gating.

Combining (3.9) and (3.3) and rewriting, one obtains

$$\sigma(f) = \frac{4\pi r_{\mathrm{t}}^2 r_{\mathrm{r}}^2}{r_{\mathrm{d}}^2} \frac{P_{\mathrm{r}}(f)}{P_{\mathrm{d}}(f)}. \tag{3.10}$$

(3.10) can be rewritten in terms of the measured calibrated RCS amplitude component $A_{\mathrm{ij}}(f)$

$$A_{\mathrm{ij}}(f) = \frac{2\sqrt{\pi} r_{\mathrm{t}} r_{\mathrm{r}}}{r_{\mathrm{d}}} \frac{V_{\mathrm{ij,r}}(f)}{V_{\mathrm{ij,d}}(f)}, \tag{3.11}$$

where $V_{\mathrm{ij,d}}(f)$ is the complex-valued amplitude as measured at the receiver for the direct path measurement.

(3.11) can be simplified if the measured object is placed at the midpoint between the transmitting and receiving antennas, *i.e.*, if $r_{\mathrm{t}} = r_{\mathrm{r}} = r_{\mathrm{d}}/2$,

$$A_{\mathrm{ij}}(f) = \frac{\sqrt{\pi} r_{\mathrm{d}}}{2} \frac{V_{\mathrm{ij,r}}(f)}{V_{\mathrm{ij,d}}(f)}, \tag{3.12}$$

where the calibration vector, $v_{\mathrm{cal}}(f)$, can be identified as

$$v_{\mathrm{cal}}(f) = \frac{\sqrt{\pi} r_{\mathrm{d}}}{2 V_{\mathrm{ij,d}}(f)}. \tag{3.13}$$

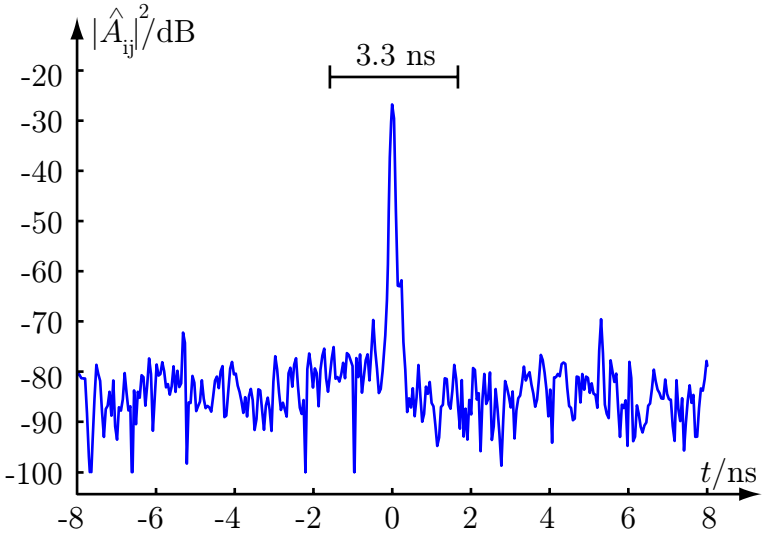

Figure 8: Time domain plot of the measurement of the forward RCS for a 10 mm radius metal sphere.

3.2.3 Comparison and discussion of calibration methods

A comparison between the two methods is made by performing forward RCS measurements on small metal spheres and calibrating the measured data with both calibration methods. The calibration object is a sphere with radius 6 cm as described in Section 3.5.

The results of the comparison measurement is shown in Figure 4. The first calibration method using a calibration target gives a more accurate result. In fact, the data calibrated in this way is so close to the theoretical results that the curve can not be distinguished from the theoretical curve in the figure.

The second method using the direct path signal to calibrate the measured data gives a rather good result with a maximum deviation from the theoretical curve of 0.7 dB. At present, it is not clear what causes this discrepancy. However, this method is attractive for practical reasons so it would be of interest to investigate the source of the discrepancy.

The first method, using a calibration target, is chosen for the measurements that we present in this report because of the better accuracy.

3.3 Background subtraction

Software or hardware gating is used in a monostatic measurement to reduce the contribution from echoes that are not in the measurement gate. The method can be used to remove echoes from the back wall and the antenna to antenna coupling. However, it cannot be used to remove unwanted echoes that are at the same distance from the radar as the target. For this reason coherent background subtraction is commonly used to suppress background clutter in monostatic RCS measurements,

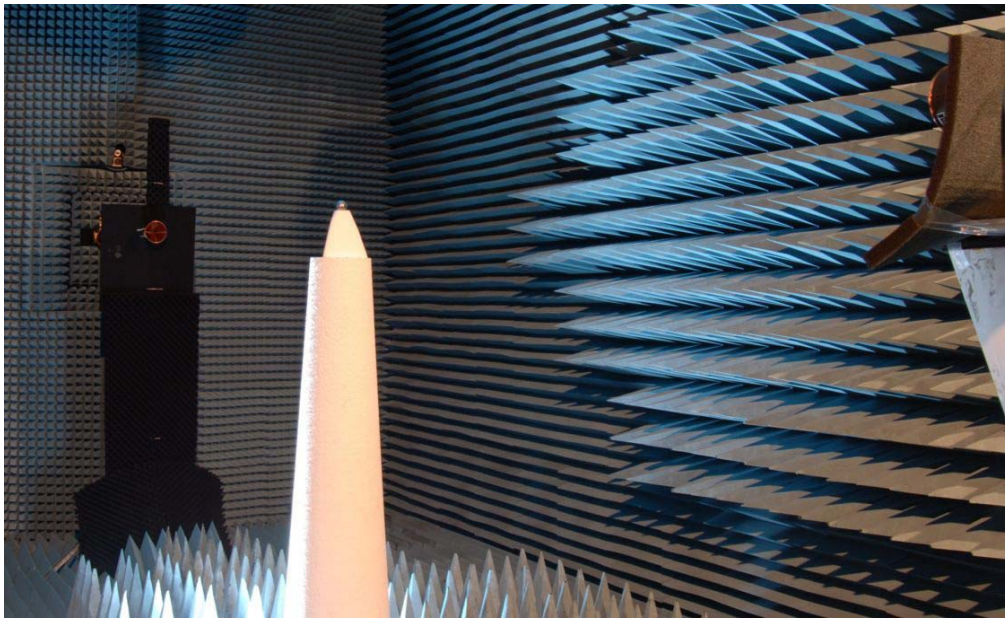

Figure 9: Photograph of the anechoic chamber setup for forward RCS measurements. From left to right: transmitting antenna, EPS column for the sample to be measured, and receiving antenna.

see Ref 9.

In a forward RCS experiment the situation is different. The antenna to antenna coupling is then within the measurement gate in these measurements which means it cannot be removed by time gating. Efficient coherent background subtraction then becomes crucial to the success for a forward RCS measurement. The stability of the system or rather, the lack of stability *i.e.*, the drift with time will effectively limit the effectiveness of the background subtraction.

Measurements are performed in order to investigate the long time stability of the forward RCS measurement system. To do this consecutive background measurements of the forward scattering amplitude, $A_{\mathrm{bg}}(f, \hat{\boldsymbol{k}})$, are performed to determine the efficiency of the background subtraction as a function of time. $A_{\mathrm{bg},0}(f, \hat{\boldsymbol{k}})$ is the forward scattering amplitude measured at $t = t_0$ and $A_{\mathrm{bg,n}}(f, \hat{\boldsymbol{k}})$ is the forward scattering amplitude measured at $t = t_n$ with $t_n > t_0$. The subtraction efficiency is defined according to (3.14). Here $\eta(f_0, t_{\mathrm{n}})$ is the subtraction efficiency for the frequency $f = f_0$ at time $t = t_n$. The efficiency is obtained by averaging over a frequency interval centered at $f = f_0$ with m frequency points.

$$\eta(f_0, t_{\mathrm{n}}) = \frac{1}{m} \sum_{f=f_0-\Delta f}^{f_0+\Delta f} \left| \frac{A_{\mathrm{bg,n}}(f, \hat{\boldsymbol{k}}) - A_{\mathrm{bg},0}(f, \hat{\boldsymbol{k}})}{A_{\mathrm{bg,n}}(f, \hat{\boldsymbol{k}})} \right|^2 \tag{3.14}$$

Figure 5 shows the subtraction efficiency, η, as a function of time for six different, 2 GHz wide, frequency bands. The measurements are performed on two different days. The bands with 6, 12 and 18 GHz center frequencies are measured at the

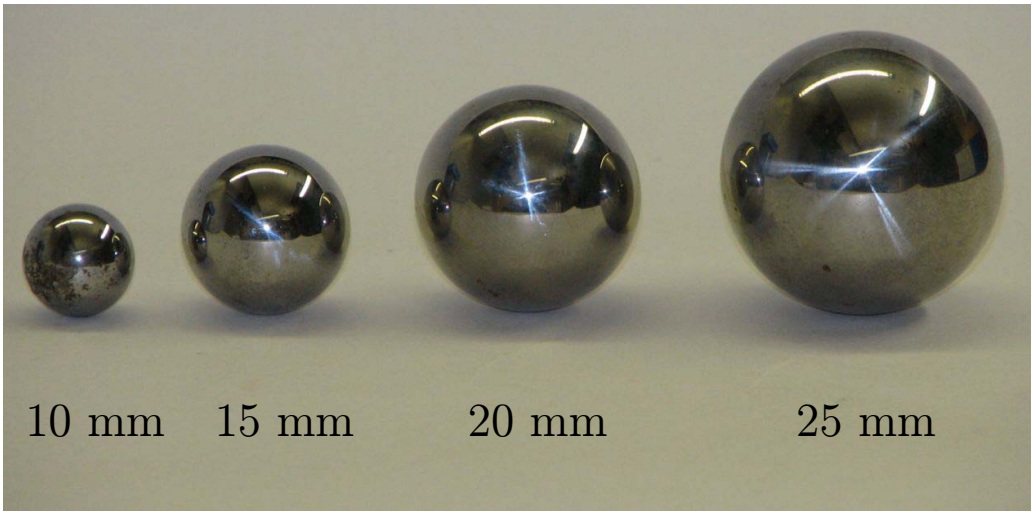

Figure 10: The picture shows the metal spheres with different radii that are used in the measurements.

same time and the bands with 24, 30 and 36 GHz center frequencies are measured at the same time but on another day.

As expected and seen in the figure, the subtraction is most efficient at low frequencies. With reduced wavelength, the effect of displacements becomes larger. The system losses, *e.g.*, cable losses, also increase with increased frequency which means a reduced signal to noise ratio (SNR). The reduced SNR reduces the efficiency of the subtraction. The figure shows that the background subtraction is most efficient if the subtraction is performed within a few minutes relative to t_0. Focusing on the first 4 h of the measurements it is seen that the curves are not monotonically increasing. Instead, the subtraction is more efficient at $t = 4\,\mathrm{h}$ than at $t = 2\,\mathrm{h}$.

The cause of the reduction of the efficiency of the background subtraction is interpreted as due to a change in distance between transmitting and receiving antenna. This interpretation is confirmed by a corresponding phase shift in the background measurement data. It is likely that this change in distance is caused by small chamber contractions or expansions due to temperature changes. Estimates of the temperature changes that are required to obtain these results can be made assuming a 6.8 m antenna to antenna distance, a chamber steel support structure and a coefficient of linear expansion of $11.7 \cdot 10^{-6}/^{\circ}\mathrm{C}$ for steel, see Ref. 15. The subtraction efficiency is –63 dB for the 6 GHz curve at $t = 2\,\mathrm{h}$ and –30 dB for the 36 GHz curve at $t = 3\,\mathrm{h}$. Assuming that the background subtraction efficiency is limited by relative displacements of the antennas, displacements of 5.6 μm and 24 μm are calculated for 6 GHz and 36 GHz, respectively. Using the antenna to antenna distance and the coefficient for linear expansion for steel, the error levels correspond to temperature changes of 0.07 °C and 0.3 °C, respectively. This means that it is extremely important to maintain a stable temperature if a good background subtraction efficiency is desired.

The result of a forward RCS measurement of the empty chamber is shown in

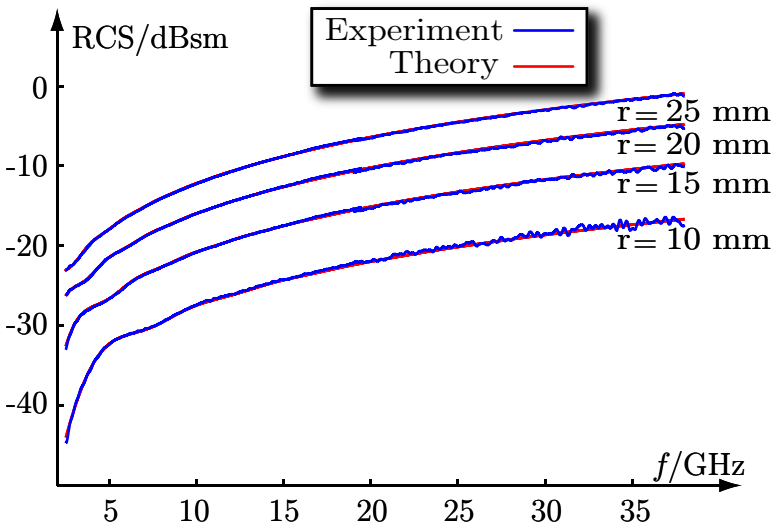

Figure 11: Measured forward RCS for metal spheres with different radii. The theoretical RCS determined from a Mie series calculation is also shown.

Figure 6. The figure also shows the results after coherent background subtraction and time domain gating. The background subtraction suppresses the background by more than 65 dB which gives a background level of less than –50 dBsm at the lower frequencies. The background suppression becomes gradually less efficient with increasing frequency and gives a background of less than –20 dBsm at the highest frequencies. Time domain gating reduces the background by another 10 dB for the lower frequencies and 15 dB for the higher frequencies.

The combined effect of coherent background subtraction and time domain gating is then to suppress the background by 75 dB at low frequencies and by 50 dB at high frequencies. This results in a remaining background level of –60 dBsm at low frequencies and –35 dBsm at high frequencies.

3.4 Time domain gating

Coherent background subtraction reduces the level of the background for all measurement distances. However, strong returns can still remain in the background after subtraction. Time domain gating, also denoted range gating can be used if the unwanted return and the target return are separated in time, *i.e.*, in range, see Ref 9. The gating can be done in hardware, so called hardware gating, by pulsing the RF signal from the radar. It can also be performed in software, so called software gating, by taking a discrete inverse fourier transform of the recorded frequency domain data, $A_{ij}(f)$.

$$\hat{A}_{ij}(t) = \mathrm{IFFT}\{A_{ij}(f)\} \tag{3.15}$$

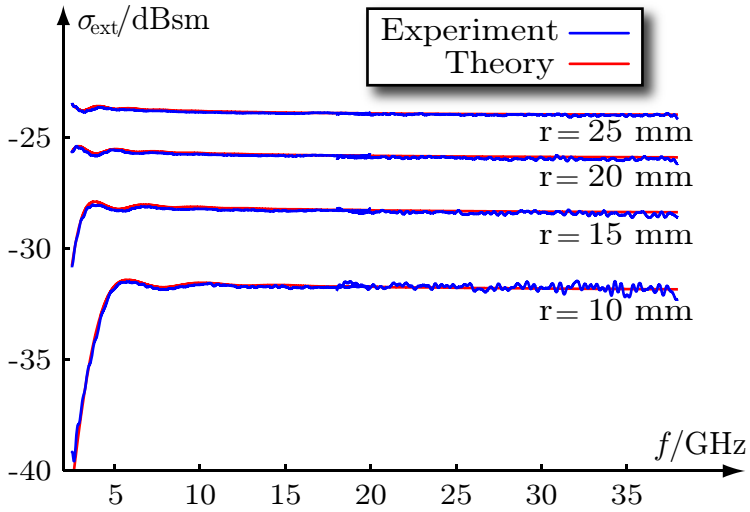

Figure 12: Measured extinction cross section for metal spheres with different radii. The theoretical extinction cross section determined from a Mie series calculation is also shown.

A window is then applied to the resulting time domain data, $\hat{A}_{\mathrm{ij}}(t)$, and $\hat{A}_{\mathrm{ij,gat}}(t)$ is obtained. The result is then transformed back to the frequency domain.

$$A_{\mathrm{ij,gat}}(f) = \mathrm{FFT}\{\hat{A}_{\mathrm{ij,gat}}(t)\} \tag{3.16}$$

The results from a forward RCS measurement on a metal sphere with 10 mm radius are shown in Figure 7. The figure also shows the result after coherent background subtraction and time domain gating.

Figure 8 shows the time domain data and the extent of the gate that was used to obtain the gated data in in Figure 7.

Different window types, both Hanning and rectangular, are tested but the results are very similar for both windows. It should also be noted here that it is important that the window is sufficiently large so that it contains the entire response of the target.

3.5 Experimental setup

This section sums up the experimental details and the measurement results presented in this report.

The forward RCS measurements are performed in an anechoic chamber, see Figures 1 and 9. A pair of wideband ridged horn antennas are positioned facing each other at a distance of 6.80 m with the sample placed on an expanded polystyrene (EPS) column at the midpoint. The measurement uses a Performance Network Analyzer (PNA) transmitting a continuous wave without online hardware or software gating. The source power from the PNA is set to 1 mW for the measurements described here. The power output from the antenna is significantly lower mainly

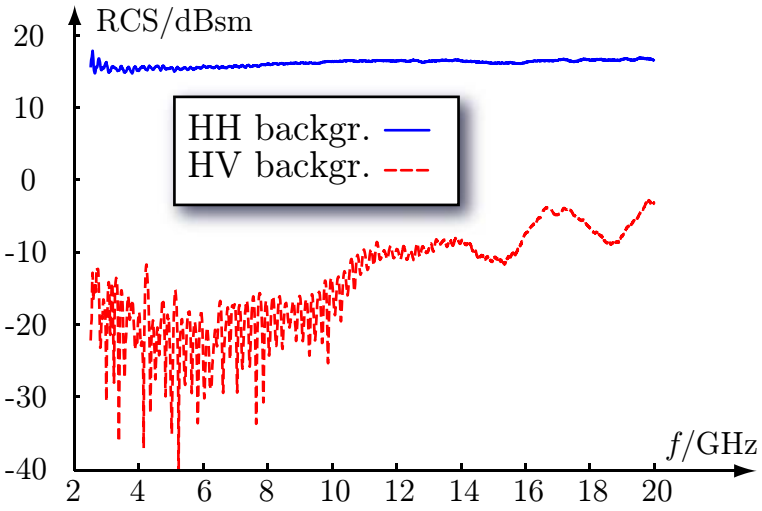

Figure 13: The figure shows the measured calibrated backgrounds for HH and HV polarizations before background subtraction.

due to cable losses. Separate measurements using two different antenna pairs are performed for the frequency intervals $[1, 22]$ GHz and $[16, 40]$ GHz.

Each interval is swept using 4000 frequency points. Eight such sweeps are averaged for each of the sample measurement, background measurement and calibration measurement. The averaging serves to improve the signal to noise ratio.

The calibration is performed either with a 60 mm radius metal sphere for the lower frequency range, $[1, 22]$ GHz, or with a 30 mm radius metal sphere for the higher frequency range, $[16, 40]$ GHz. The calibration measurement with the sphere is preceded and followed by measurements of the background that are averaged and coherently subtracted from the calibration object measurement. The Mie series result for a perfectly electric conducting sphere, see Ref. 17, is divided by the background subtracted calibration data to obtain a calibration vector.

The sample is then measured and the background is subtracted from the sample data in the same way as for the calibration measurement. The background measurements are performed within less than 1 minute before/after each measurement to minimize the influence of the background.

The background subtracted sample data is finally calibrated and time domain gated. The window size is chosen to minimize the influence of the background but containing the complete response from the target. In the measurements on the small steel spheres a 3.3 ns gate is used. An 18 ns gate is used for the measurements on the helix which has an extended response. The time domain filtering and a large antenna beam width at low frequencies reduce the useful frequency range to $[2.5, 38]$ GHz.

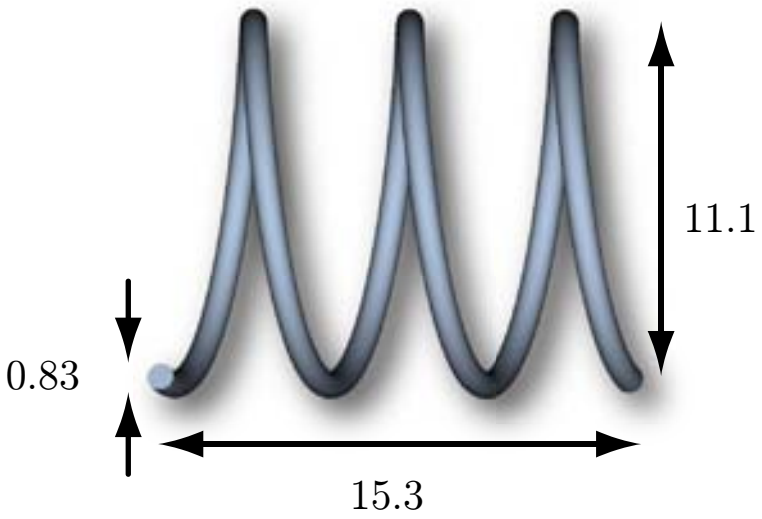

Figure 14: Drawing of the helix sample. The dimensions, in mm, are shown in the figure.

4 Results and discussion

Some measurements are performed to further investigate the performance of the experimental setup. The results are compared with theoretical calculations. The experimental results are used to determine the accuracy of the forward RCS measurements and the following determination of extinction cross section. Polarimetric measurements are also performed by measuring for linear polarizations and combining the results to obtain circular polarizations.

4.1 Wideband measurements

Tests of the accuracy of the method to determine the forward RCS are performed by measurements on metal high precision ball bearing spheres with 10 mm, 15 mm, 20 mm, and 25 mm radii for the [2.5, 38] GHz frequency range, see Fig 10.

The RCS is measured in the forward direction and the extinction cross section is determined using the optical theorem, (2.6).

The results are shown in Figures 11 and 12. The forward RCS and the extinction cross sections obtained from the Mie series are shown for reference in the figures. The largest discrepancy between measurement and theory for the extinction cross section is found for the 10 mm radius sphere where it is less than 0.5 dB at –31 dBsm.

4.2 Polarimetric measurements

The cross-polarization distortion in the transmit and receive channels can be estimated measuring the background signal using the setup in Figure 1 without a target. Figure 13 shows the results from such a measurement of the calibrated background

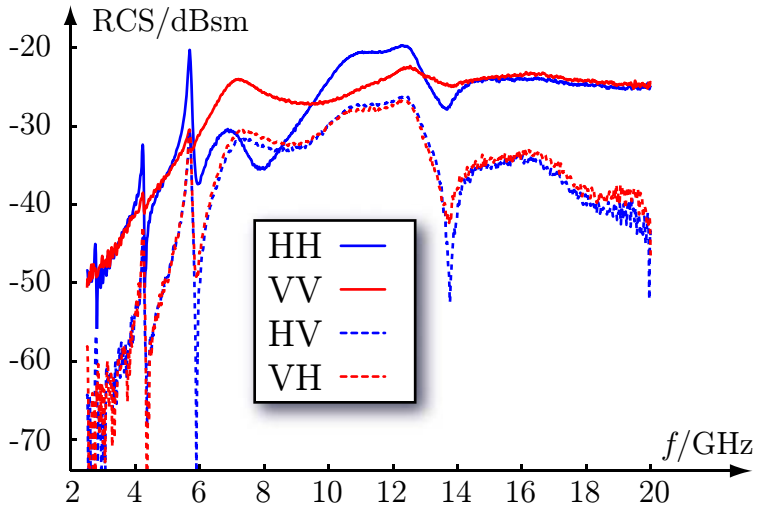

Figure 15: The figure shows the measured linearly polarized forward RCS components.

signal for the HH and HV components. The suppression, *i.e.*, the difference between the two curves, varies from approximately 20 dB to more than 30 dB depending on frequency.

The forward RCS of a helix, see Figure 14, is measured with the incident wave direction, $\hat{\boldsymbol{k}}$, along the axis of the helix. A helix is chosen because it is expected to give different extinction cross sections for different circular polarizations of the incident wave. The four linearly polarized components, HH, VV, HV and VH, of the forward RCS obtained from a measurement of the helix sample are shown in Figure 15. The corresponding forward components of the RCS amplitude are used to determine the circular polarized components. The LL and RR forward RCS components are shown in Figures 16 and 17, respectively. The results are compared with method-of-moments calculations to validate the method. It is found that the measured and calculated results qualitatively agree well.

The corresponding forward RCS amplitude components can be used with (2.6) to obtain extinction cross sections for circular polarized incident waves. The resulting extinction cross sections for the helix for left circular polarized incident wave and for a right circular polarized incident wave are shown in Figures 18 and 19, respectively. There is also, as expected, a large difference between the two polarizations due to the geometry of the helix. The results are also here compared with method-of-moments calculations.

Polarimetric calibration to reduce the effect of cross-polarization distortion in the transmit and receive channels is considered for future development of the method presented in this paper. One could *e.g.*, use methods analogous to polarimetric calibration methods suggested for monostatic measurements. One should then use at least two calibration targets with significant cross-polarization return and known scattering matrix, see Ref. 22. A straightforward implementation is found in Ref. 7 where a dihedral reflector is used for polarimetric calibration of monostatic RCS

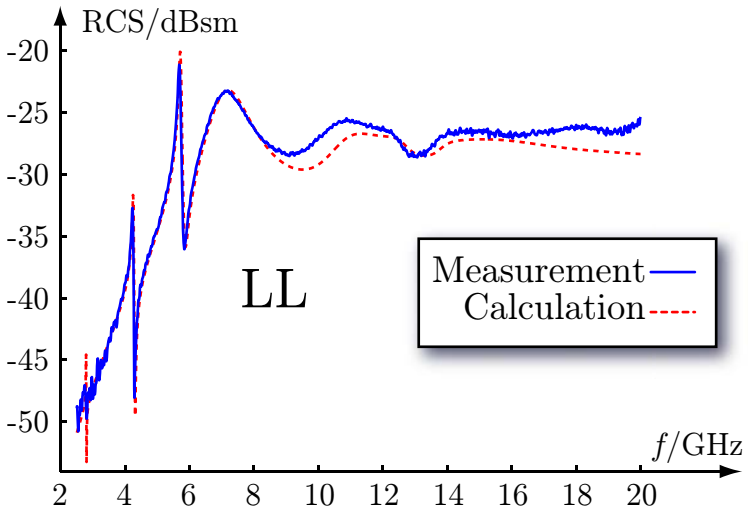

Figure 16: The figure shows the forward RCS for LL-polarization determined from experiments and calculations.

measurements. However, finding a calibration object for broadband forward scattering polarimetric calibration is more complicated than in the monostatic case.

5 Conclusions

A method to determine the extinction cross section utilizing forward RCS measurements is developed. It is used to determine the extinction cross section with good accuracy for general objects for the frequency range [2.5, 38] GHz.

The method presented in this paper can be used for arbitrary polarization of the incident radiation for targets smaller than 0.16 m up to 18 GHz and smaller than 0.11 m up to 38 GHz. It is found that a calibration using a calibration target is more accurate than an alternative calibration method that does not require a calibration target. It is concluded that the alternative method needs further analysis to be useful for this purpose.

It is suggested that changes in the relative distance from transmitting antenna to receiving antenna are the limiting factor for the background subtraction efficiency. Software time domain gating can be used to suppress echoes that do not emanate from the target but care has to taken so that the entire target response is included in the gate. It is found that the combined effect of coherent background subtraction and time domain gating is to suppress the background by 75 dB at low frequencies and by 50 dB at high frequencies. This results in a remaining background level of –60 dBsm at low frequencies and –35 dBsm at high frequencies for a forward RCS measurement.

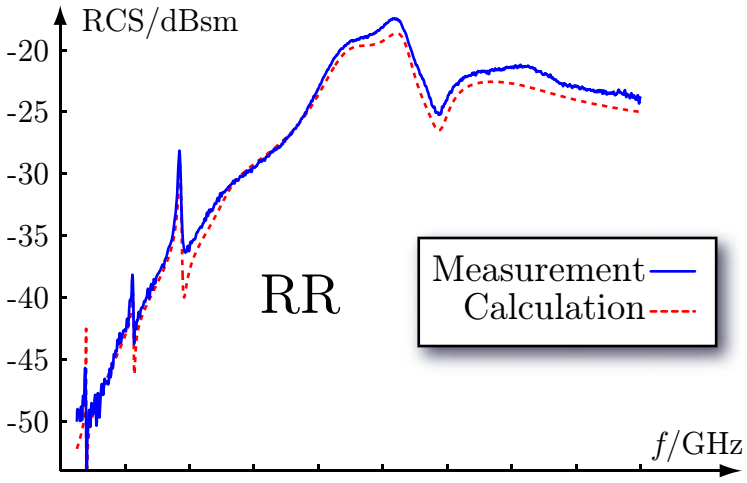

Figure 17: The figure shows the forward RCS for RR-polarization determined from experiments and calculations.

The method is validated by measuring small metal spheres with known extinction cross sections. It is determined that the extinction cross section can be measured with good accuracy down to a level of –30 dBsm for the investigated frequency range. Measurements of the RCS amplitude linear polarization components can be used to calculate the extinction cross section for a circular polarized incident wave.

Acknowledgments

The financial support by the Swedish Research Council, the Swedish Foundation for Strategic Research and the Swedish Defense Materiel Administration is gratefully acknowledged. We would also like to acknowledge the technical assistance from Mats Andersson at Saab Bofors Dynamics.

References

[1] P. Beckmann and A. Spizzichino. *The scattering of electromagnetic waves from rough surfaces*. Pergamon, Oxford, 1963.

[2] C. F. Bohren and D. R. Huffman. *Absorption and Scattering of Light by Small Particles*. John Wiley & Sons, New York, 1983.

[3] M. Cherniakov, R. Abdullah, P. Jancovic, M. Salous, and V. Chapursky. Automatic ground target classification using forward scattering radar. *IEE Proceedings Radar, Sonar and Navigation*, **153**(5), 427–437, 2006.

[4] M. G. Cote. Automated swept-angle bistatic measurement system. Technical Report RL-TR-93-52, Rome Laboratory, Rome Laboratory/ERCT, 31 Grenier Street, Hansom AFB MA 01731-3010, 1993. http://stinet.dtic.mil.

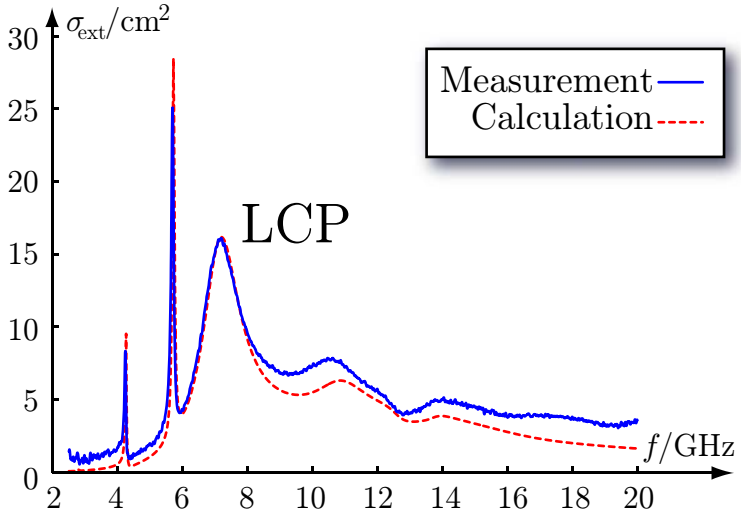

Figure 18: The figure shows the extinction cross sections, $\sigma_{\text{ext}}(f)$, for left circular (LCP) polarization of the incident wave determined from experiments and calculations.

[5] N. C. Currie. *Techniques of radar reflectivity measurement.* Artech House, Dedham, 1989.

[6] F. Daout, A. Khenchaf, and J. Saillard. Calibration of bistatic polarimetric scatterometers. In *Geoscience and Remote Sensing Symposium, 1996. IGARSS '96. 'Remote Sensing for a Sustainable Future.', International*, volume 1, pages 746–748 vol.1, May 1996.

[7] J.-R. J. Gau and W. D. Burnside. New polarimetric calibration technique using a single calibration dihedral. *IEE Proc. Microwaves, Antennas and Propagation*, **142**(1), 19–25, 1995.

[8] M. Gustafsson and C. Sohl. New physical bounds on elliptically polarized antennas. In *Proceedings of the Third European Conference on Antennas and Propagation*, pages 400–402, Berlin, Germany, March 23–27 2009. The Institution of Engineering and Technology.

[9] IEEE recommended practice for radar cross-section test procedures, 2007. IEEE Std 1502-2007.

[10] IEEE standard radar definitions, 2008. IEEE Std 686-2008 (Revision of IEEE Std 686-1997).

[11] E. F. Knott, J. F. Shaeffer, and M. T. Tuley. *Radar Cross Section.* SciTech Publishing Inc., 5601 N. Hawthorne Way, Raleigh, NC 27613, 2004.

[12] W. E. Kock. Related experiments with sound waves and electromagnetic waves. *Proceedings of the IRE*, **47**(7), 1192–1201, July 1959.

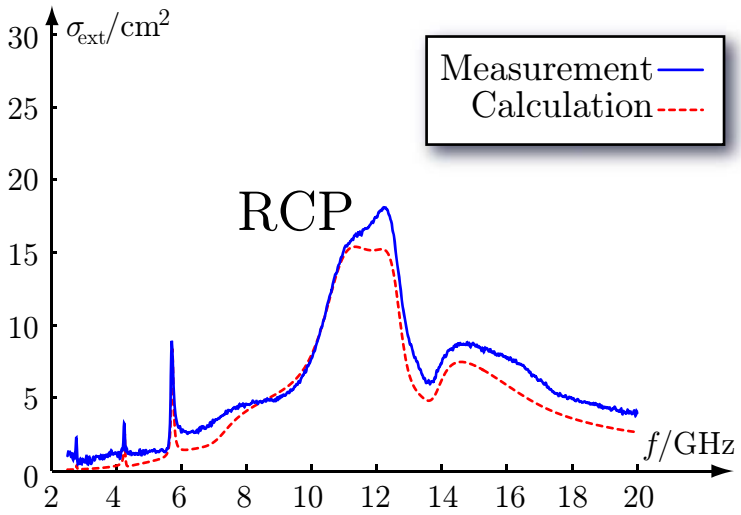

Figure 19: The figure shows the extinction cross sections, $\sigma_{\text{ext}}(f)$, for right circular (RCP) polarization of the incident wave determined from experiments and calculations.

[13] R. G. Kouyoumjian and L. Peters. Range requirements in radar cross-section measurements. *Proceedings of the IEEE*, **53**(8), 920–928, 1965.

[14] C. Larsson, C. Sohl, M. Gustafsson, and G. Kristensson. Wideband extinction measurements for thin and planar samples. Technical Report LUTEDX/(TEAT-7166)/1–10/(2008), Lund University, Department of Electrical and Information Technology, P.O. Box 118, S-221 00 Lund, Sweden, 2008. http://www.eit.lth.se.

[15] D. R. Lide. *CRC handbook of chemistry and physics : a ready-reference book of chemical and physical data. Ed. 88 (2007-2008)*. CRC Press, Boca Raton, Florida, 2008.

[16] R. Newton. Optical theorem and beyond. *Am. J. Phys*, **44**, 639–642, 1976.

[17] G. T. Ruck, D. E. Barrick, W. D. Stuart, and C. K. Krichbaum. *Radar Cross-Section Handbook*, volume 1 and 2. Plenum Press, New York, 1970.

[18] M. I. Skolnik. An analysis of bistatic radar. *IRE Transactions on Aeronautical and Navigational Electronics*, **ANE-8**(1), 19–27, March 1961.

[19] M. I. Skolnik. *Introduction to radar systems*. McGraw-Hill, Boston, 3rd edition, 2001.

[20] C. Sohl, M. Gustafsson, and G. Kristensson. Physical limitations on broadband scattering by heterogeneous obstacles. *J. Phys. A: Math. Theor.*, **40**, 11165–11182, 2007.

[21] C. Sohl, C. Larsson, M. Gustafsson, and G. Kristensson. A scattering and absorption identity for metamaterials: experimental results and comparison with theory. *J. Appl. Phys.*, **103**(5), 054906, 2008.

[22] B. M. Welsh, B. M. Kent, and A. L. Buterbaugh. Full polarimetric calibration for radar cross-section measurements: Performance analysis. *IEEE Trans. Antennas Propagat.*, **52**(9), 2357–2365, 2004.

[23] N. J. Willis. *Bistatic Radar*. Artech House, Boston, London, 1991.

[24] E. Zdansky. Kalibrering av radarmålarea, särskilt objektfri kalibrering. Technical Report FOI-R-2442-SE, Defence Research Establishment, Division of Sensor Technology, PO Box 1165, SE-581 11 Linköping, Sweden, 2007. http://www.foi.se.

[25] E. Zdansky and A. Örbom. Prov med objektfri kalibrering av radarmålarea. Technical Report FOI-R-2443-SE, Defence Research Establishment, Division of Sensor Technology, PO Box 1165, SE-581 11 Linköping, Sweden, 2007. http://www.foi.se.